Published in final edited form as:
Circ Res. 2013 March 1; 112(5): 755–761. doi:10.1161/CIRCRESAHA.111.300576.

Polymeric nanoparticle PET/MR imaging allows macrophage detection in atherosclerotic plaques

Maulik D. Majmudar[1,2,*], **Jeongsoo Yoo**[1,3,*], **Edmund J. Keliher**[1], **Jessica Truelove**[1], **Yoshiko Iwamoto**[1], **Brena Sena**[1], **Partha Dutta**[1], **Anna Borodovsky**[4], **Kevin Fitzgerald**[4], **Marcelo Di Carli**[5], **Peter Libby**[2], **Daniel G. Anderson**[6,7,8], **Filip K. Swirski**[1], **Ralph Weissleder**[1,9], and **Matthias Nahrendorf**[1]

[1]Center for Systems Biology, Massachusetts General Hospital, 185 Cambridge St, Boston, MA 02114

[2]Cardiovascular Division, Department of Medicine, Brigham and Women's Hospital, Boston, MA

[3]Department of Molecular Medicine, Kyungpook National University School of Medicine, Daegu, South Korea

[4]Alnylam Pharmaceuticals, 300 3rd Street, Cambridge, MA 02142

[5]Division of Nuclear Medicine and Molecular Imaging, Department of Radiology, Brigham and Women's Hospital, 75 Francis Street, Boston, MA

[6]David H. Koch Institute for Integrative Cancer Research, Massachusetts Institute of Technology, 77 Massachusetts Avenue, Cambridge, MA, 02139

[7]Department of Chemical Engineering, MIT

[8]Division of Health Science Technology, MIT

[9]Department of Systems Biology, Harvard Medical School, 200 Longwood Avenue, Boston, MA 02115

Abstract

Rationale—Myeloid cell content in atherosclerotic plaques associates with rupture and thrombosis. Thus, imaging of lesional monocyte and macrophages (Mo/Mϕ) could serve as a biomarker of disease progression and therapeutic intervention.

Objective—To noninvasively assess plaque inflammation with dextran nanoparticle-facilitated hybrid PET/MR imaging.

Methods and Results—Using clinically approved building blocks, we systematically developed 13nm polymeric nanoparticles consisting of crosslinked short chain dextrans which were modified with desferoxamine for zirconium-89 radiolabeling (^{89}Zr-DNP) and a near infrared fluorochrome (VT680) for microscopic and cellular validation. Flow cytometry of cells isolated from excised aortas showed DNP uptake predominantly in Mo/Mϕ (76.7%) and lower signal originating from other leukocytes such as neutrophils and lymphocytes (11.8% and 0.7%, $p<0.05$ versus Mo/Mϕ). DNP colocalized with the myeloid cell marker CD11b on immunohistochemistry.

Corresponding Author: Ralph Weissleder, MD, PhD, Matthias Nahrendorf, MD, PhD, Center for Systems Biology, Massachusetts General Hospital, 185 Cambridge St, Boston, MA, 02114, Phone: 617-643-0500, Fax: 617-643-6133, mnahrendorf@mgh.harvard.edu.
*These authors contributed equally

Disclosures
Anna Borodovsky and Kevin Fitzgerald are full time employees at Alnylam. Daniel Anderson holds Alnylam shares.

PET/MRI revealed high uptake of ^{89}Zr-DNP in the aortic root of ApoE$^{-/-}$ mice (standard uptake value, ApoE$^{-/-}$ mice versus wild type controls, 1.9±0.28 versus 1.3±0.03, $p<0.05$), corroborated by ex vivo scintillation counting and autoradiography. Therapeutic silencing of the monocyte-recruiting receptor CCR2 with siRNA decreased ^{89}Zr-DNP plaque signal ($p<0.05$) and inflammatory gene expression ($p<0.05$).

Conclusions—Hybrid PET/MR imaging with a 13nm DNP enables noninvasive assessment of inflammation in experimental atherosclerotic plaques and reports on therapeutic efficacy of anti-inflammatory therapy.

Keywords

PET/MRI; inflammation; atherosclerosis; molecular imaging; nanoparticles

INTRODUCTION

During atherogenesis, monocytes and macrophages invade the arterial intima, and sustain and amplify local inflammation through secretion of cytokines, reactive oxygen species, and proteolytic enzymes[1]. These innate immune cells may differentiate into foam cells and favor degradation of extracellular matrix macromolecules and thinning of the fibrous cap, features of plaques that have ruptured and triggered myocardial infarction or stroke[2]. Macrophage-targeted imaging may provide the opportunity to detect upstream events that play a causative role in disease progression, and thus enable preventive therapy[3, 4]. Iron oxide nanoparticle uptake assessed by magnetic resonance imaging (MRI) has began to address this need[3, 4], but this approach is mostly semiquantitative, and the detection sensitivity for these nanoparticles is about 50-times lower compared to radioisotope imaging[5].

This study aimed to develop a sensitive, clinically viable technique for detection of inflammatory leukocytes in atherosclerotic plaque with positron emission tomography (PET). The approach used core-free dextran nanoparticles (DNP) made from clinically approved components, labeled with desferoxamine to chelate the PET isotope zirconium-89. Dextran is biocompatible and biodegradable, making it a suitable starting material for nanoparticles intended for clinical use. We tested dextran nanoparticles using hybrid PET/MR imaging for detecting macrophages in atherosclerotic plaques in ApoE$^{-/-}$ mice. MRI provided the anatomic reference for the source of the PET signal, which reported on nanoparticle deposition in the vessel wall. We further employed the PET macrophage reporter ^{89}Zr-DNP to assess the efficacy of a therapeutic intervention: monocyte/macrophage-targeted RNA interference. Using lipidoid nanoparticle-enabled silencing of CCR2[6], the chemokine receptor that dominates recruitment of inflammatory monocytes[7], we followed plaque inflammation with PET/MRI non-invasively and related imaging results to modified gene expression patterns in the vascular wall.

METHODS

Dextran nanoparticle synthesis

Dextran (10 kDa; Amersham Biosciences, Sweden) was cross-linked with epichlorohydrin followed by partial amination with ethylene diamine to yield amino-dextran nanoparticles[8]. DNP-NH2 was modified with p-isothiocyanatobenzyl desferoxamine (SCN-Bz-Df; Macrocyclics, TX) and the N-hydroxysuccinimidyl ester of the near-infrared fluorochrome VivoTag680 (VT680; PerkinElmer, Waltham, MA). The remaining amines were succinylated. The quantitative radiolabeling of the nanoparticle was achieved at room temperature by complexation with zirconium-89 (^{89}Zr) to give ^{89}Zr-DNP. The

radiochemical yield and purity of ^{89}Zr-DNP were determined using radio-TLC using ITLC plates and 50 mM EDTA as a mobile phase.

Short-interfering RNA (siRNA) nanoparticle synthesis

siRNA synthesis and formulation into lipoid nanoparticles used previously described methods. The RNA duplex for silencing CCR2 was 5′-uGcuAAAcGucucuGcAAAdTsdT-3′ (sense), 5′-UUUG cAGAGACGUUuAGcAdTsdT -3′ (anti-sense), a sequence known to limit CCR2 expression[6]. Single-strand RNAs were produced, annealed and used as duplexes. The nanocarrier for siRNA delivery was prepared with a cationic lipid using a spontaneous vesicle formation procedure[6]. Lipids were dissolved in 90% ethanol and mixed with siRNA solution (1:1 ratio) at fixed speed and diluted immediately with phosphate buffered saline (PBS) to final 25% ethanol concentration. The ethanol was then removed and the external buffer replaced with PBS by dialysis.

Animal experiments

Female C57Bl/6 (n=10) and apolipoprotein E knock out (ApoE$^{-/-}$) mice (n=22) were purchased from The Jackson Laboratory (Jackson, MI). C57Bl/6 (B6) mice were 12–16 weeks of age. ApoE$^{-/-}$ mice had an average age of 28 weeks and consumed a high-cholesterol diet (HCD; Harlan Teklad, 0.2% total cholesterol) for at least 16 weeks, conditions that reliably produce atherosclerotic plaques in the aortic root and arch. Mice were anesthetized for all procedures (isoflurane 1.5%; O_2 2 L/min). Animal experiments were approved by Massachusetts General Hospital's Institutional Subcommittee on Research Animal Care.

Treatment protocols

To test ^{89}Zr-DNP as a biomarker of therapeutic efficiency, we treated a cohort of ApoE$^{-/-}$ mice with tail vein injections of siRNA targeting CCR2 (siCCR2, n=5) or siRNA targeting luciferase as control (siCON, n=5) at a dose[6] of 0.5 mg/kg. Mice were age-matched, and allocated randomly to groups (siCON versus siCCR2).

Flow Cytometry

ApoE$^{-/-}$ mice were euthanized 24 hours after injection of DNP (5 nmol VT680) for flow cytometry analysis (n=3–4 per group). Aortas were excised under a dissecting microscope and minced in medium containing 450 U/ml collagenase I, 125 U/ml collagenase XI, 50 U/ml DNase I, and 60 U/ml hyaluronidase (Sigma-Aldrich), and incubated at 37 °C for 1 hour with agitation at 750 rpm. Aortas were processed in PBS with 0.5% bovine serum albumin and 1% fetal bovine serum (FACS buffer). The processed single cell suspensions (300 μl) were stained with fluorochrome-labeled antibodies (BD Biosciences) against mouse leukocyte markers as follows: a Phycoerythrin (PE) anti-mouse lineage antibody cocktail containing antibodies directed against CD90, B220, CD49b, NK1.1, Ly-6G, and Ter-119 was used. Myeloid cells were then stained with anti-mouse CD11b, F4/80, and Ly-6C. Monocytes were defined as (CD90/B220/CD49b/NK1.1/Ly-6G/Ter-119)^{low}, CD11b^{high}, F4/80^{low}, Ly-6C$^{low/high}$. Macrophages were defined as (CD90/B220/CD49b/NK1.1/Ly-6G/Ter-119)^{low}, CD11b^{high}, F4/80^{high}, Ly-6C^{int}. Neutrophils were defined as (CD90/B220/CD49b/NK1.1/Ly-6G/Ter-119)^{high} and CD11b^{high}. Lymphocytes were defined as (CD90/B220/CD49b/NK1.1/Ly-6G/Ter-119)^{high} and CD11b^{low}. Flow cytometry was performed on a multicolor flow cytometer (LSR II, BD Biosciences).

Histologic evaluation

Histologic examination of aortic roots was performed 24 hours after injection of DNP-VT680. Aortas were excised, rinsed in PBS, embedded in OCT compound (Sakura Finetek)

and flash-frozen in a 2-methylbutane bath with dry ice. Fresh-frozen 6–10 μm thick serial sections were prepared and immunohistochemically stained for the myeloid cell marker CD11b (clone: M1/70, BD Biosciences). On adjacent sections, immunofluorescence staining was performed to analyze microscopic DNP distribution and colocalization with CD11b positive cells. The sections were stained with FITC-CD11b (clone: M1/70, BD Biosciences) and the slides were coverslipped using a mounting medium with DAPI (Vector Laboratories Inc.). Fluorescence microscopy was performed using a Nikon Eclipse 80i equipped with a Cascade Model 512B camera (Roper Scientific), a Cy5.5 filter cube (HQ650/45x EX, dichroic Q680LP BS, and HQ710/50m EM), a FITC filter cube (HQ480/40x EX, dichroic Q505LP BS, HQ535/50m EM), and a UV filter cube (D365/10x EX, dichroic 380DCLP BS, E400LPv2 EM) (Chroma Technology Corp.). Capturing of images of stained sections used a digital slide scanner, NanoZoomer 2.0RS (Hamamatsu, Japan).

Biodistribution and Autoradiography

The blood half-life of ^{89}Zr-DNP was determined with serial retroorbital bleeds after injection of 150 μCi of ^{89}Zr-DNP into the tail vein of five B6 mice. After sacrifice (48 hours), mice were perfused with 10 ml of phosphate-buffered saline. Organs were harvested, weighed, and their activity was recorded with a gamma counter (1480 Wizard 3-inch PerkinElmer, Waltham, MA). Biodistribution data were corrected for radioactive decay and residual radioactivity at the injection site. Oil-Red-O staining depicted the distribution of plaques in ApoE$^{-/-}$ aortas that were subsequently photographed by a digital camera as well as analyzed by digital autoradiography. Aortas were exposed to a phosphorimager plate and read with a Typhoon FLA9000 system (GE Healthcare) 4 hours later. Visualization of scanned autoradiography images was performed using the ImageJ program (Image J 1.440, NIH, Bethesda, MD).

Quantitative RT-PCR

Messenger RNA was extracted from the aortic root and arch using a RNeasy Micro Kit (Qiagen) using manufacturer's protocol. One microgram of mRNA was used to generate complimentary DNA (cDNA) using a high capacity RNA to cDNA kit (Applied Biosystems). cDNA was then further amplified using the QuantiTect Whole Transcriptome kit (Qiagen). The amplified cDNA was diluted at a ratio of 1:10 in DNase- and RNase-free H_2O and 2 μL of final cDNA was used for further analysis. Levels of mRNAS encoding target genes used Taqman assays (Applied Biosystems). Variability in cDNA concentration was normalized using GAPDH, a constitutively expressed gene.

PET-CT imaging

Imaging experiments were performed 48 hours after injection of ^{89}Zr-DNP at 354±13 μCi/mouse. All PET-CT images were acquired on a Siemens Inveon micro PET-CT. Each PET acquisition was ~90 minutes in duration. PET was reconstructed from 600 million coincidental 511 keV photon counts. Counts were rebinned in 3D by registering photons spanning no more than 3 consecutive rings, then reconstructed into sinograms by using a high resolution Fourier Rebin algorithm. Image pixel size was anisotropic, with dimensions of 0.796 mm in the z direction and 0.861 mm in the x and y directions, for a total of 128 × 128 × 159 pixels. Data are expressed as standard uptake values (SUV), which normalize radioactivity for body weight and injected dose. Blood signal was used to calculate the target to background ratio.

CT images were reconstructed from 360 projections of X-rays with a cone beam angle of 9.3 degrees over 360 degrees perpendicular to the animal bed. 80 keV X-rays were transmitted from a 500 μA anode source, 347 mm from the center of rotation and recorded on a CCD detector, containing 2048 transaxial and 3072 axial pixels. Isotropic CT pixel size was 110.6

μm, with a total of 512 × 512 × 768 pixels. Projections were acquired at end expiration using a BioVet gating system (M2M Imaging, Cleveland, OH) and CT acquisition time was ~10 minutes. Reconstruction of data sets used IRW software (Siemens).

PET/MR registration and fusion

In vivo MRI was performed for anatomic reference immediately after PET/CT imaging in ApoE$^{-/-}$ mice with or without siCCR2 treatment. Cine images were obtained on a 7-Tesla Bruker Pharmascan with electrocardiogram and respiratory gating (SA instruments, Inc., Stony Brook, NY) using a fast gradient echo FLASH sequence with the following parameters: echo time 2.7 ms; 16 frames per R-R interval (repetition time 7.0 to 15.0 ms); resolution 200 μm × 200 μm × 1 mm; number of excitations 4; flip angle 60°. PET/CT and MR images were acquired sequentially using a custom-designed mouse bed and a PET-CT gantry adapter[9]. Offline fusion was based on external fiducial markers. A custom-built mouse vest of several loops of PE50 tubing was filled with 15% iodine in water, visible in both CT and MRI. PET data were fused to CT as part of a standard PET-CT workflow. Registration of MRI and PET-CT data sets was then obtained by superimposing the fiducial landmarks with AMIRA software (Version 5.4, Berlin, Germany)[9].

Statistics

Results are expressed as mean ± SEM. Differences between groups were evaluated by Student's t-test. We used GraphPad Prism 4.0c for Macintosh (GraphPad Software Inc.) for statistical analysis. A p value of <0.05 was used to indicate statistical significance.

RESULTS

Nanoparticle preparation, blood half-life, and biodistribution

The core-free nanoparticles used in this study consisted of polymeric dextran and had a mean particle size of 13.3 nm as determined by laser light scattering. On average, 8 desferoxamine and 1 fluorochrome moieties were attached per particle. The radiolabeling yield of ^{89}Zr-DNP (Fig. 1A, B) was > 99.5%. After centrifugation, the radiochemical purity was 100%. ^{89}Zr-DNP was injected into five C57Bl/6 mice to measure the nanoparticle's kinetics in vivo. ^{89}Zr-DNP had a blood half-life of 3.73 ± 0.33 hours (R^2 of fit = 0.95; Figure 1C). Biodistribution of ^{89}Zr-DNP at 48 hours was as follows (expressed as %ID/g): liver, 11.1 ± 1.4; spleen, 10.3 ± 1.8; lymph node, 5.3 ± 0.9; blood, 4.7 ± 1.0; kidney, 3.4 ± 0.2; heart, 1.2 ± 0.2; aorta, 1.2 ± 0.1; tail, 0.9 ± 0.2; lung, 1.0 ± 0.4; intestines, 0.9 ± 0.1; fat, 0.6 ± 0.1; and muscle, 0.4 ± 0.1 (Figure 1D).

In vivo hybrid PET/MR imaging of ^{89}Zr-DNP detects atherosclerotic plaque inflammation

^{89}Zr-DNP uptake in atherosclerotic aortic root plaques was quantified with PET, while MRI provided the anatomical reference. The aortic root and arch of ApoE$^{-/-}$ mice had significantly higher activity compared to wild type controls (standard uptake value 1.85±0.28 versus 1.25±0.03, and 1.46±0.09 versus 0.98±0.04; $p<0.05$ for both; Figure 2A and 2B). The target-to-blood background ratio in aortic root and arch of ApoE$^{-/-}$ mice also significantly exceeded that in wild type controls (aortic root and arch, 2.56±0.19 versus 1.64±0.03, and 2.16±0.34 versus 1.29±0.07; $p<0.05$ for both).

Ex vivo scintillation counting and autoradiography confirm in vivo PET/MRI

After imaging, we measured radioactivity in excised aortas by scintillation counting and autoradiography exposure. Compared to wild type, the percent injected dose per gram tissue (%ID/g) was significantly higher in aortas harvested from ApoE$^{-/-}$ mice (0.69±0.09 versus 1.24±0.11, $p<0.01$, Figure 2C). Autoradiography showed the peak activity in the aortic root

and arch. Oil-Red-O stained lipid-rich plaques correlated well with the peak isotope signal on autoradiography (Figure 2D).

DNP accumulate in plaque leukocytes

Nanoparticle uptake into atherosclerotic plaques in the aortic root was assessed using fluorescence microscopy (Figure 3). Microscopic images of adjacent sections stained for the mononuclear phagocyte antigen CD11b showed colocalization of myeloid cells with DNP in aortic root plaques (Figure 3A and 3B). CD11b is expressed primarily by monocytes, macrophages and neutrophils. Imaging of sections in the lower-wavelength FITC channel confirmed the specificity of the observed signal for nanoparticles rather than autofluorescence (Figure 3C). Higher magnification immunofluorescent microscopy after immunoreactive staining with CD11b corroborated colocalization of the DNP signal to $CD11b^{+}$ cells (Figure 3D–F).

Cellular sources of the nanoparticle signal

Quantification of DNP uptake into specific leukocyte populations (monocytes, macrophages, neutrophils and lymphocytes) used multicolor flow cytometry detection of cell surface markers and the fluorochrome-labeled nanoparticle taken up by respective cells. Aortas were excised and cells isolated 24 hours after injection of DNP. Single cell suspensions were stained with an antibody cocktail for specific leukocyte cell surface markers, and the fluorescence signal of DNP was compared for different cells. Flow cytometry revealed that the majority of DNP accumulated in Mo/Mϕ (Figure 4), however, 23% of the cellular signal derived from other sources. This observation suggests that while the majority of the PET signal in atherosclerotic plaques resulted from uptake of nanoparticles by Mo/Mϕ, DNP was not entirely specific for those cells but also taken up to some degree by neutrophils and lymphocytes. Of note, flow cytometry does not detect extracellular signal.

PET/MRI detects therapeutic effects of in vivo RNAi

Further experiments assessed the utility of ^{89}Zr-DNP PET/MRI for following the efficacy of a therapeutic intervention: silencing of CCR2, the monocytic chemokine receptor responsible for migration of the inflammatory monocyte subset to sites of inflammation using short-interfering RNA (siRNA) technology. siRNA silencing of CCR2 (siCCR2) significantly attenuated receptor protein expression in circulating and splenic monocytes[6]. This intervention lowered the PET/MRI ^{89}Zr-DNP signal in association with attenuated monocyte recruitment. The aortic roots of siCCR2 treated $ApoE^{-/-}$ mice had decreased PET signal when compared to $ApoE^{-/-}$ mice treated with an irrelevant siRNA. The target-to-background ratio changed from 2.25 ± 0.11 to 1.82 ± 0.10; $p<0.03$ (Figures 5A and 5B).

After imaging, quantitative reverse-transcriptase PCR (qRT-PCR) of aortic extracts assessed gene expression. Systemic silencing of CCR2 reduced the expression of genes involved in vascular inflammation. Expression of CCR2, vascular cell adhesion molecule-1 (VCAM1), interleukin-6 (IL-6), and tumor necrosis factor-alpha (TNFα) fell in siCCR2 treated mice, while transforming growth factor-beta (TGFβ) and arginase (Arg1) gene expression rose (Figure 5C).

Discussion

Timely identification of patients with high risk for myocardial infarction or stroke remains challenging. It is even more difficult to predict the risk of rupture for a specific atherosclerotic plaque, a thrombotic trigger tightly linked to inflammation. Identification of inflamed atheromata could trigger aggressive risk factor modification, intensive pharmacologic treatment, and perhaps other preemptive interventions to enhance lesion

stability and reduce the probability of plaque rupture and thrombosis. Thus, techniques for assessment of plaque inflammation might aid prevention of myocardial infarction and stroke. Inflammatory monocytes and macrophages play a central role in the pathobiology of plaque complication. Since these cells elaborate matrix-degrading proteases implicated in plaque rupture, they furnish attractive imaging biomarkers for plaque instability. The current work focused on the detection of inflammatory myeloid cells in atheromata with clinically viable, radioisotope labeled dextran nanoparticles without a metal core. Hybrid PET/MRI detection of these nanoparticles permitted tracking of RNAi-mediated silencing of CCR2, a chemokine receptor that mediates the recruitment of inflammatory monocytes into the arterial intima.

Prior studies have used PET for macrophage imaging[3], especially with fluorodeoxyglucose (^{18}F-FDG)[10, 11]. PET has interest for detection of cellular and molecular targets, because it is the most sensitive noninvasive clinical imaging technology, and permits quantitation[4]. ^{18}F-FDG has widespread clinical availability, and studies have correlated ^{18}F-FDG uptake to the macrophage content of atheromata[10, 11]. Yet, ^{18}F-FDG uptake lacks specificity for macrophages. Many other cells, including cardiomyocytes, smooth muscle cells and other leukocytes, all of which are present in or close to atherosclerotic plaques, accumulate high amounts of glucose, making specific imaging of plaque inflammation with ^{18}F-FDG challenging in the coronary arteries. A recent study showed that hypoxia, but not pro-inflammatory cytokines, augments glucose uptake by human macrophages[12]. Thus, there is an unmet need for more specific macrophage-targeted imaging agents. In contrast to ^{18}F-FDG, DNP report on phagocytic rather than metabolic activity. In the current work, 13 nm dextran nanoparticles were designed for clinical translatability. These nanoparticles are composed of clinically approved materials, including small crosslinked dextran strands, and do not contain a metal core, hence they are not detectable with MRI. Modified with desferoxamine, a clinically approved metal chelator, the nanoparticles were labeled with zirconium-89 for PET imaging. Zirconium-89 has a slow radioactive decay matching the in vivo kinetics of the 13 nm DNP. Therefore, imaging can be done after the nanoparticle has cleared from the blood pool yielding a low background signal. DNP could also be labeled with other PET isotopes. If a smaller particle size accelerated pharmacokinetics, shorter injection-imaging sequences may facilitate fluorine-18 labeling. Importantly, ^{89}Zr-DNP are easily biodegradable, supporting translation to humans.

While PET and MR imaging was done sequentially and data were fused offline in our study, newer scanners allow for synchronous data acquisition in mice and in patients[13]. Our data highlight the advantages of combining both modalities. MRI is a leading modality for imaging the cardiovascular system, and may thus prove to be particularly useful in conjunction with PET. Sparse molecular or cellular targets can be quantitated by PET, while MRI delivers high-contrast, high-resolution, and time-resolved cardiovascular imaging without additional radiation exposure. This approach permits analysis of molecular targets in anatomical and physiological context, as MRI may deliver information on tissue motion and strain, blood flow, oxygenation, diffusion, and fiber orientation[14, 15]. PET/MRI could also enable dual target molecular imaging by simultaneous use of MRI agents. For example, one could use ^{89}Zr-DNP for imaging of inflammation in conjunction with MR agents that detect cell death[16], collagen[17] or fibrin deposition[18].

Preclinical and clinical studies have highlighted the role of chronic persistent inflammation in the pathophysiology of atherosclerosis, hence specific anti-inflammatory therapy might produce clinical benefit. Here, we encapsulated short-interfering RNA in lipidoid nanoparticles for delivery to phagocytic cells. The target was CCR2, a receptor for the chemokine MCP-1 that specifically recruits the inflammatory monocyte subset to sites of inflammation in mice and in humans[7]. As shown in landmark studies on the role of this

chemokine/chemokine receptor axis, deficiency of either CCR2[19] or MCP-1[20] prevents recruitment of monocytes, thereby reducing macrophage burden and inflammation in plaques. We previously validated the delivery of siRNA to circulating and splenic monocytes by lipidoid nanoparticles and the efficiency of CCR2 silencing for the RNA target sequence[6]. The splenic monocyte reservoir[21] is a particularly suitable target, as these cells rapidly ingest lipidoid nanoparticles used for siRNA delivery[6]. In atherosclerotic mice, the spleen contributes monocytes to atherosclerotic plaque[22]. Our current study followed monocyte-targeted siRNA therapy by plaque macrophage PET/MR imaging. We found significantly reduced PET signal in the aortic root and arch of $ApoE^{-/-}$ mice treated with siCCR2. The decreased macrophage PET signal was accompanied by a significantly reduced inflammatory gene expression pattern in the imaged arterial bed. The expression of CCR2 and several other pro-inflammatory genes fell, whereas the mRNAs that encode TGF-β and arginase, genes associated with resolution of inflammation, increased. Future studies will clarify if ^{89}Zr-DNP PET/MRI will be useful for imaging of therapeutic efficiency.

In conclusion, this study demonstrates the feasibility of nanoparticle-facilitated hybrid PET/MR imaging of inflammatory leukocytes in murine atherosclerotic plaques. The majority of cellular ^{89}Zr-DNP signal (77% by flow cytometry) was derived from monocytes/macrophages, hence the cellular specificity was limited. Specific targeting of monocyte recruitment with RNAi reduced the macrophage PET signal and dampened inflammation in plaques. Clinical translation of this cellular imaging strategy could identify macrophage-rich plaques at risk for complications and evaluate the effectiveness of macrophage-targeted therapies in atheromata.

Acknowledgments

We gratefully acknowledge Matt Sebas (CSB imaging core, MGH), the medium scale synthesis group for preparing the CCR2 siRNA, Will Cantley for making the liposomal formulation, Victor Koteliansky, Tatiana Novobrantseva for helpful discussions (Alnylam).

Sources of Funding

This project has been funded in part with Federal funds from the National Heart, Lung, and Blood Institute, National Institutes of Health, Department of Health and Human Services (HHSN268201000044C, R01-HL096576, R01-HL095629, and T32-HL094301).

Non-standard Abbreviations and Acronyms

Arg1	arginase 1
CCR2	C-C chemokine receptor type 2
DNP	dextran nanoparticles
FDG	fluorodeoxyglucose
IL6	interleukin 6
MCP1	monocyte chemotactic protein 1
MI	myocardial infarction
Mo/Mϕ	monocytes and macrophages
MRI	magnetic resonance imaging
PET	positron emission tomography
siRNA	short-interfering RNA

TGFβ	transforming growth factor beta
TNFα	tumon necrosis factor - alpha
VCAM1	vascular cell adhesion molecule 1

References

1. Libby P. Inflammation in atherosclerosis. Nature. 2002; 420:868–874. [PubMed: 12490960]
2. Swirski FK. The spatial and developmental relationships in the macrophage family. Arterioscler Thromb Vasc Biol. 2011; 31:1517–1522. [PubMed: 21677294]
3. Sanz J, Fayad ZA. Imaging of atherosclerotic cardiovascular disease. Nature. 2008; 451:953–957. [PubMed: 18288186]
4. Nahrendorf M, Sosnovik DE, French BA, Swirski FK, Bengel F, Sadeghi MM, Lindner JR, Wu JC, Kraitchman DL, Fayad ZA, Sinusas AJ. Multimodality cardiovascular molecular imaging, Part II. Circ Cardiovasc Imaging. 2009; 2:56–70. [PubMed: 19808565]
5. Nahrendorf M, Zhang H, Hembrador S, Panizzi P, Sosnovik DE, Aikawa E, Libby P, Swirski FK, Weissleder R. Nanoparticle PET-CT imaging of macrophages in inflammatory atherosclerosis. Circulation. 2008; 117:379–387. [PubMed: 18158358]
6. Leuschner F, Dutta P, Gorbatov R, Novobrantseva TI, Donahoe JS, Courties G, Lee KM, Kim JI, Markmann JF, Marinelli B, Panizzi P, Lee WW, Iwamoto Y, Milstein S, Epstein-Barash H, Cantley W, Wong J, Cortez-Retamozo V, Newton A, Love K, Libby P, Pittet MJ, Swirski FK, Koteliansky V, Langer R, Weissleder R, Anderson DG, Nahrendorf M. Therapeutic siRNA silencing in inflammatory monocytes in mice. Nat Biotechnol. 2011; 29:1005–1010. [PubMed: 21983520]
7. Charo IF, Ransohoff RM. The many roles of chemokines and chemokine receptors in inflammation. N Engl J Med. 2006; 354:610–621. [PubMed: 16467548]
8. Keliher EJ, Yoo J, Nahrendorf M, Lewis JS, Marinelli B, Newton A, Pittet MJ, Weissleder R. 89Zr-labeled dextran nanoparticles allow in vivo macrophage imaging. Bioconjug Chem. 2011; 22:2383–2389. [PubMed: 22035047]
9. Lee WW, Marinelli B, van der Laan AM, Sena BF, Gorbatov R, Leuschner F, Dutta P, Iwamoto Y, Ueno T, Begieneman MP, Niessen HW, Piek JJ, Vinegoni C, Pittet MJ, Swirski FK, Tawakol A, Di Carli M, Weissleder R, Nahrendorf M. PET/MRI of inflammation in myocardial infarction. J Am Coll Cardiol. 2012; 59:153–163. [PubMed: 22222080]
10. Figueroa AL, Subramanian SS, Cury RC, Truong QA, Gardecki JA, Tearney GJ, Hoffmann U, Brady TJ, Tawakol A. Distribution of inflammation within carotid atherosclerotic plaques with high-risk morphological features: a comparison between positron emission tomography activity, plaque morphology, and histopathology. Circ Cardiovasc Imaging. 2012; 5:69–77. [PubMed: 22038986]
11. Myers KS, Rudd JH, Hailman EP, Bolognese JA, Burke J, Pinto CA, Klimas M, Hargreaves R, Dansky HM, Fayad ZA. Correlation between arterial FDG uptake and biomarkers in peripheral artery disease. JACC Cardiovasc Imaging. 2012; 5:38–45. [PubMed: 22239891]
12. Folco EJ, Sheikine Y, Rocha VZ, Christen T, Shvartz E, Sukhova GK, Di Carli MF, Libby P. Hypoxia but not inflammation augments glucose uptake in human macrophages: Implications for imaging atherosclerosis with 18fluorine-labeled 2-deoxy-D-glucose positron emission tomography. J Am Coll Cardiol. 2011; 58:603–614. [PubMed: 21798423]
13. Sauter AW, Wehrl HF, Kolb A, Judenhofer MS, Pichler BJ. Combined PET/MRI: one step further in multimodality imaging. Trends Mol Med. 2010; 16:508–515. [PubMed: 20851684]
14. Dall'Armellina E, Karamitsos TD, Neubauer S, Choudhury RP. CMR for characterization of the myocardium in acute coronary syndromes. Nat Rev Cardiol. 2010; 7:624–636. [PubMed: 20856263]
15. Goergen CJ, Sosnovik DE. From molecules to myofibers: multiscale imaging of the myocardium. J Cardiovasc Transl Res. 2011; 4:493–503. [PubMed: 21643889]
16. Burtea C, Ballet S, Laurent S, Rousseaux O, Dencausse A, Gonzalez W, Port M, Corot C, Vander Elst L, Muller RN. Development of a magnetic resonance imaging protocol for the

characterization of atherosclerotic plaque by using vascular cell adhesion molecule-1 and apoptosis-targeted ultrasmall superparamagnetic iron oxide derivatives. Arterioscler Thromb Vasc Biol. 2012; 32:e36–48. [PubMed: 22516067]

17. Klink A, Heynens J, Herranz B, Lobatto ME, Arias T, Sanders HM, Strijkers GJ, Merkx M, Nicolay K, Fuster V, Tedgui A, Mallat Z, Mulder WJ, Fayad ZA. In vivo characterization of a new abdominal aortic aneurysm mouse model with conventional and molecular magnetic resonance imaging. J Am Coll Cardiol. 2011; 58:2522–2530. [PubMed: 22133853]
18. Makowski MR, Forbes SC, Blume U, Warley A, Jansen CH, Schuster A, Wiethoff AJ, Botnar RM. In vivo assessment of intraplaque and endothelial fibrin in ApoE(−/−) mice by molecular MRI. Atherosclerosis. 2012; 222:43–49. [PubMed: 22284956]
19. Boring L, Gosling J, Cleary M, Charo IF. Decreased lesion formation in CCR2−/− mice reveals a role for chemokines in the initiation of atherosclerosis. Nature. 1998; 394:894–897. [PubMed: 9732872]
20. Gu L, Okada Y, Clinton SK, Gerard C, Sukhova GK, Libby P, Rollins BJ. Absence of monocyte chemoattractant protein-1 reduces atherosclerosis in low density lipoprotein receptor-deficient mice. Mol Cell. 1998; 2:275–281. [PubMed: 9734366]
21. Swirski FK, Nahrendorf M, Etzrodt M, Wildgruber M, Cortez-Retamozo V, Panizzi P, Figueiredo JL, Kohler RH, Chudnovskiy A, Waterman P, Aikawa E, Mempel TR, Libby P, Weissleder R, Pittet MJ. Identification of splenic reservoir monocytes and their deployment to inflammatory sites. Science. 2009; 325:612–616. [PubMed: 19644120]
22. Robbins CS, Chudnovskiy A, Rauch PJ, Figueiredo JL, Iwamoto Y, Gorbatov R, Etzrodt M, Weber GF, Ueno T, van Rooijen N, Mulligan-Kehoe MJ, Libby P, Nahrendorf M, Pittet MJ, Weissleder R, Swirski FK. Extramedullary hematopoiesis generates Ly-6C(high) monocytes that infiltrate atherosclerotic lesions. Circulation. 2012; 125:364–374. [PubMed: 22144566]

Novelty and Significance

What Is Known?

- Macrophages, effector cells of innate immunity, can destabilize atherosclerotic plaques by secreting pro-inflammatory cytokines and proteases.
- Macrophages associate with plaque rupture, and triggering of myocardial infarction and stroke in patients with atherosclerosis.
- Nanoparticles, avidly taken up by macrophages, may report on, a plaque's propensity to provoke a thrombotic complication.

What New Information Does This Article Contribute?

- Nanoparticles made from dextran building blocks accumulate in macrophages resident in atherosclerotic plaque.
- Derivatization of these particles with the radioactive isotope zirconium-89 enables imaging of aortic plaques of apoE$^{-/-}$ mice by positron emission tomography.
- In vivo silencing of CCR2, the receptor that monocytes rely on for recruitment to sites of inflammation, reduces the nanoparticle imaging signal in concert with attenuated inflammatory gene expression.

Many ischemic complications arise from atherosclerotic plaques that do not significantly obstruct blood flow. Conventional anatomic imaging can therefore not predict which lesions are at high risk of rupture. Such information could guide individual risk assessment and direct preventive therapy. The present work describes the use of 13nm dextran nanoparticles for imaging plaque inflammation in mice with atherosclerosis. Nanoparticles were derivatized with a radioactive isotope and detected by positron emission tomography, joined with magnetic resonance imaging for anatomic reference. Mice with silenced monocyte chemokine receptor CCR2 accumulated fewer inflammatory cells in atherosclerotic lesions, in parallel with reduced expression of inflammatory genes. Translation of this technology could enable identification of patients at risk for plaque rupture and direct preventive measures to avoid thrombotic complications such as stroke and MI.

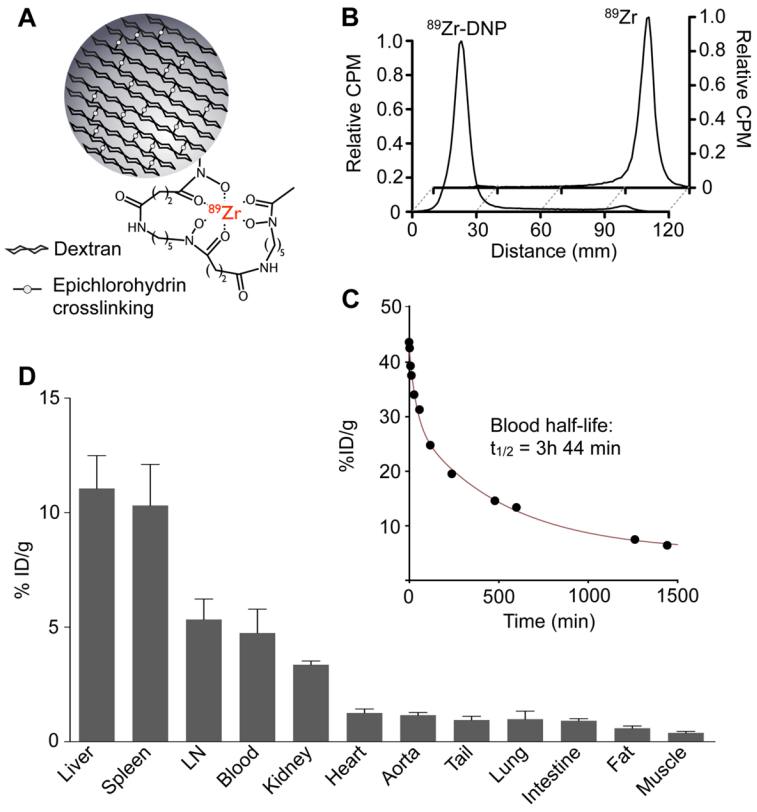

Figure 1.

Nanoparticle preparation and pharmacokinetics. A, Schematic representation of nanoparticle. B, Radio-thin layer chromatography traces for ^{89}Zr-DNP and ^{89}Zr. C, Blood half-life of ^{89}Zr-DNP. D, Biodistribution 48 hours after intravenous administration of ^{89}Zr-DNP (n=5). CPM: counts per minute, %ID/g: percent injected dose per gram tissue; LN: lymph nodes.

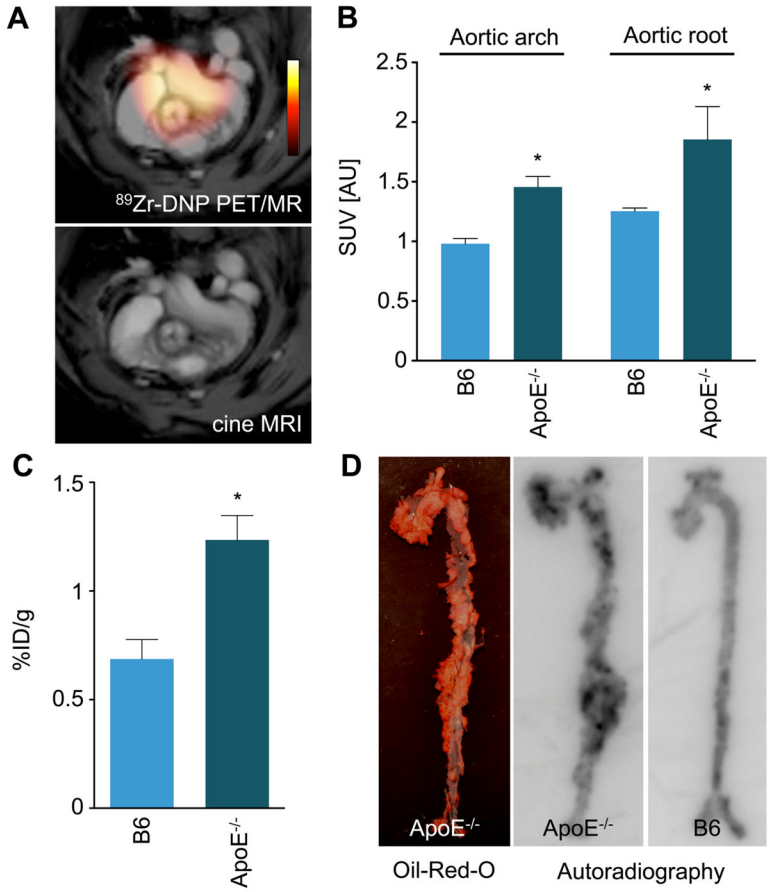

Figure 2.

Validation of ^{89}Zr-DNP imaging. A, Representative hybrid PET/MR image in ApoE$^{-/-}$ mouse. (top). Cine MRI frame of aortic valve (bottom). B, In vivo PET signal in the aortic arch and root in wild-type C57BL/B6 and ApoE$^{-/-}$ mice with atherosclerosis (n=4–5 per group). C, Scintillation counting of excised aortas corroborated data from in vivo PET/MR imaging. Data are normalized for weight, radioactive decay, and injected dose. D, Oil-Red-O staining (left panel) and autoradiography (middle and right panels) of excised aortas. %ID/g: percent injected dose per gram tissue. Data are presented as mean±SEM, *p<0.05.

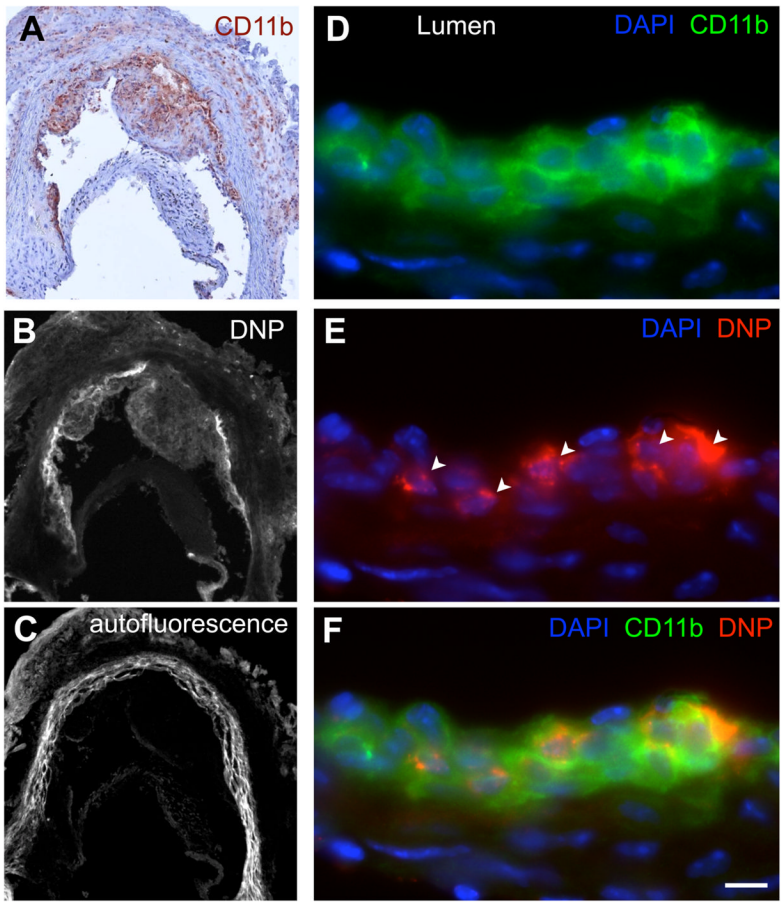

Figure 3.

DNP accumulation in atherosclerotic plaques. A, Immunohistochemical localization of $CD11b^{+}$ myeloid cells. B, Fluorescence microscopy of nanoparticle distribution in the adjacent section. C, Autofluorescence image of B. D–F, Higher magnification immunofluorescence microscopy of CD11b (D) and DNP (arrow heads in E). In the merged image (F), DNP signal occurs inside cells that stain positive for CD11b on their surface. Scale bar indicates 20 μm.

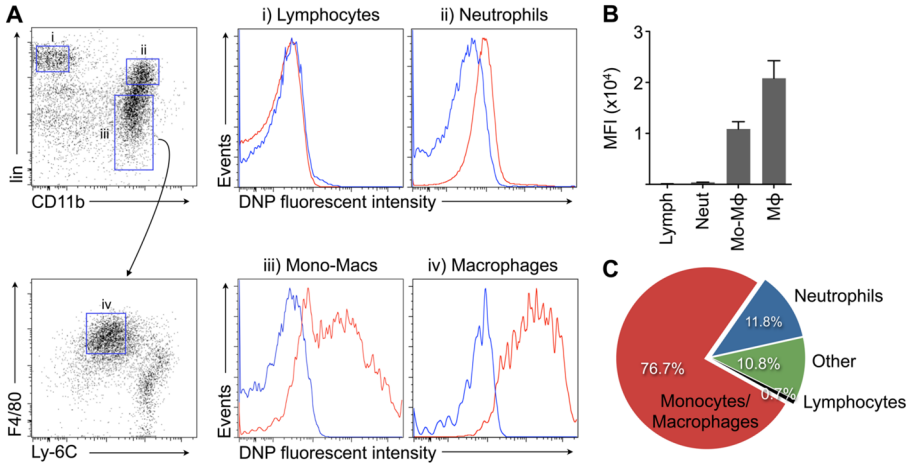

Figure 4.

Flow cytometric analysis of DNP distribution in aortic plaque. A, The plot on the far left shows gates for i) lymphocytes, ii) neutrophils, iii) mononuclear phagocytes, iv) macrophages. The histograms report their respective intracellular signal in the VT680 FACS channel, which represents nanoparticle uptake by cells. Blue histograms indicate the signal in uninjected control ApoE$^{-/-}$ mice while red lines indicate signal from cells retrieved from ApoE$^{-/-}$ mice after DNP injection (n=3 per group). B, Bar graph of mean fluorescent intensity in different leukocytes. C, Pie chart showing the relative signal contribution per cell type. Mo-Mϕ: monocytes/macrophages.

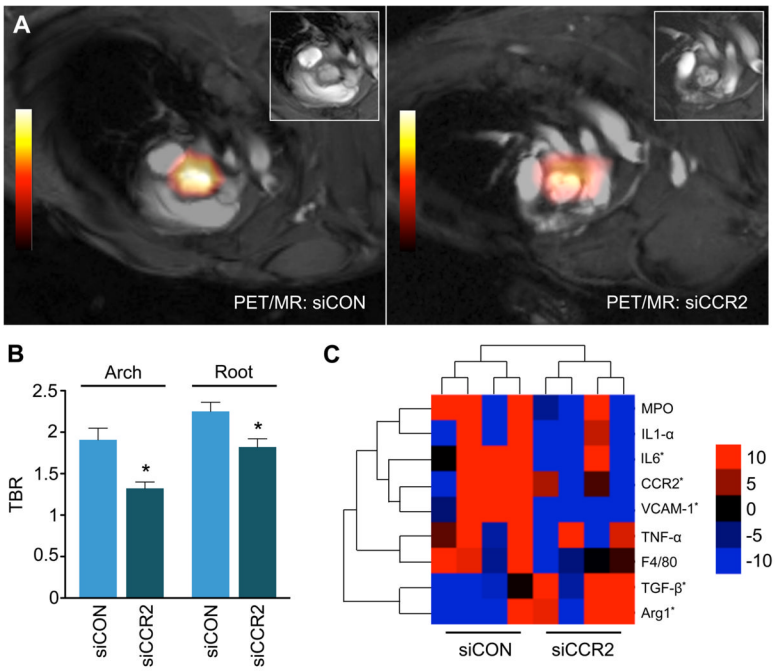

Figure 5.

PET/MRI and gene expression analysis of siRNA treated ApoE$^{-/-}$ mice. A, Representative PET/MR images of control siRNA (siCON) and siCCR2 treated ApoE$^{-/-}$ mice. Inset: MRI frame at the level of the aortic valve. B, PET target-to-background ratio in ApoE$^{-/-}$ mice treated with control siRNA (siCON) versus siCCR2 (n=5 per group). Data are presented as mean±SEM, *p<0.05. C, Heat map of genes in aortic roots (n=4 per group). Each row of the heat map represents a gene while each column represents an experimental treatment group (labeled at the bottom). The color scale represents the level of gene expression, with red indicating an increase in gene expression and blue indicating a decrease in gene expression.